

# Iron and Sulfur Precursors Affect Crystalline Structure, Speciation, and Reactivity of Sulfidized Nanoscale Zerovalent Iron

Jiang Xu, Astrid Avellan, Hao Li, Elizabeth A. Clark, Graeme Henkelman, Ralf Kaegi, and Gregory V. Lowry\*



Cite This: *Environ. Sci. Technol.* 2020, 54, 13294–13303



Read Online

ACCESS |



Metrics & More

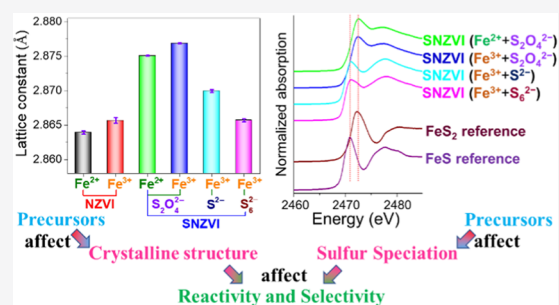


Article Recommendations



Supporting Information

**ABSTRACT:** The reactivity of sulfidized nanoscale zerovalent iron (SNZVI) is affected by the amount and species of sulfur in the materials. Here, we assess the impact of the Fe ( $\text{Fe}^{2+}$  and  $\text{Fe}^{3+}$ ) and S ( $\text{S}_2\text{O}_4^{2-}$ ,  $\text{S}^{2-}$ , and  $\text{S}_6^{2-}$ ) precursors used to synthesize both NZVI and SNZVI on the resulting physicochemical properties and reactivity and selectivity with water and trichloroethene (TCE). X-ray diffraction indicated that the Fe precursors altered the crystalline structure of both NZVI and SNZVI. The materials made from the  $\text{Fe}^{3+}$  precursor had an expanded lattice in the  $\text{Fe}^0$  body-centered-cubic (BCC) structure and lower electron-transfer resistance, providing higher reactivity with water ( $\sim 2$ – $3$  fold) and TCE ( $\sim 5$ – $13$  fold) than those made from an  $\text{Fe}^{2+}$  precursor. The choice of the S precursor controlled the S speciation in the SNZVI particles, as indicated by X-ray absorption spectroscopy. Iron disulfide ( $\text{FeS}_2$ ) was the main S species of SNZVI made from  $\text{S}_2\text{O}_4^{2-}$ , whereas iron sulfide ( $\text{FeS}$ ) was the main S species of SNZVI made from  $\text{S}^{2-}/\text{S}_6^{2-}$ . The former SNZVI was more hydrophobic, reactive with, and selective for TCE compared to the latter SNZVI. These results suggest that the Fe and S precursors can be used to select the conditions of the synthesis process and provide selected physicochemical properties (e.g., S speciation, hydrophobicity, and crystalline structure), reactivity, and selectivity of the SNZVI materials.



## 1. INTRODUCTION

Nanoscale zerovalent iron (NZVI) has been studied as an in situ groundwater remediation technology for more than two decades.<sup>1–12</sup> More recently, sulfidation of NZVI (SNZVI) has been proposed as a promising modification to greatly improve the reactivity, selectivity, and longevity of NZVI, decreasing the undesirable side reaction between  $\text{Fe}^0$  and water ( $\text{H}_2$  evolution).<sup>13–25</sup> The electron efficiency or selectivity of SNZVI for contaminants can be described as the fraction of electron equivalents from  $\text{Fe}^0$  that is used for the reduction of the target contaminant.<sup>19,26</sup> The electron efficiency for the reduction of trichloroethene (TCE) in water is  $\sim 25$ – $400$ -fold higher for SNZVI compared to NZVI.<sup>18,19,27–29</sup>

Various sulfidation methods and S precursors have been proposed to synthesize SNZVI. A typical co-sulfidation method uses  $\text{Na}_2\text{S}_2\text{O}_4$  as the sulfur precursor, which is mixed with a  $\text{NaBH}_4$  solution and then dropwise added into an aqueous solution of either  $\text{Fe}^{2+}$  or  $\text{Fe}^{3+}$ .<sup>13,30–34</sup> Alternatively, a typical postsulfidation method uses  $\text{Na}_2\text{S}$  as the sulfur precursor to sulfidize as-prepared NZVI particles.<sup>14,35–40</sup> Other approaches have also been reported, e.g., using  $\text{Na}_2\text{S}$  as a co-sulfidation reagent, using  $\text{Na}_2\text{S}_2\text{O}_4$  or thiosulfate as a postsulfidation reagent.<sup>41–44</sup> Few studies measured and reported the actual amount of S in the synthesized particles. Our recent studies have demonstrated that the actual S amount in the particles can be much lower than the dosed amount, and

that co-sulfidation incorporates more S into the materials than postsulfidation.<sup>27,28,44</sup> However, the impact of the type of Fe and S precursors on the S content of SNZVI is unknown.

Besides the S content, the S speciation is another important factor that controls the physicochemical properties of SNZVI.<sup>28</sup> In the literature, the S speciation is mainly studied using X-ray photoelectron spectroscopy (XPS), which detects S oxidation states primarily on the surface ( $< 10$  nm). This can lead to artifacts because the surface of the materials is inevitably oxidized during sample preparation for the XPS measurement. Although the reduction of the contaminants by NZVI is generally considered a surface reaction, the overall electron-transfer efficiency from the  $\text{Fe}^0$ -rich core to the reactive surface will likely be controlled by the  $\text{FeS}_x$  speciation in or on the surface of the particles, due to the different band gaps of  $\text{FeS}_x$ , e.g.,  $\text{FeS} = 0.10$  eV,  $\text{FeS}_2 = 0.95$  eV, and  $\text{Fe}_3\text{S}_4 = 0.00$  eV.<sup>45</sup> It is widely reported that an FeS (iron monosulfide) phase is either coated onto or mixed with the  $\text{Fe}^0$  phase for particles made from either co-sulfidation by  $\text{Na}_2\text{S}_2\text{O}_4$  or

Received: June 14, 2020

Revised: September 18, 2020

Accepted: September 23, 2020

Published: September 23, 2020



postsulfidation by  $\text{Na}_2\text{S}$ , mostly according to the S 2p XPS spectra and/or transmission electron microscopy coupled with energy-dispersive X-ray spectroscopy (TEM-EDX) analysis.<sup>13,41</sup> A recent study-used synchrotron-based pair distribution function (PDF) analysis found an FeS shell on the  $\text{Na}_2\text{S}_2\text{O}_4$  co-sulfidized SNZVI.<sup>46</sup> X-ray absorption spectroscopy (XAS), which provides an average S speciation in the particles (surface and interior), confirmed the predominance of FeS in the SNZVI particles made by co-sulfidation using  $\text{Na}_2\text{S}_2\text{O}_4$ .<sup>28,47</sup> However,  $\text{FeS}_2$  was recently found in the SNZVI particles with higher S content.<sup>28</sup> There is a limited understanding of whether or not different S and Fe precursors would affect the speciation of S in the SNZVI particles.

The commonly used Fe precursors ( $\text{Fe}^{2+}$  or  $\text{Fe}^{3+}$ ) for NZVI or SNZVI synthesis have not been reported to impact the properties and reactivity of the resulting particles. Differences in the reactivity of NZVI or SNZVI reported from individual research groups are most often attributed to batch-to-batch variations in the surface oxidation/passivation,  $\text{Fe}^0$  content, S content, and the available surface area. However, florfenicol was only poorly reactive after 2 h with NZVI synthesized using an  $\text{Fe}^{2+}$  precursor,<sup>16,17</sup> but it was reactive with NZVI synthesized using an  $\text{Fe}^{3+}$  precursor (Figure S1). The surface-area-normalized rate of florfenicol removal by NZVI and SNZVI synthesized using an  $\text{Fe}^{3+}$  precursor was 12 and 17 times higher than that using an  $\text{Fe}^{2+}$  precursor, respectively, under exactly the same synthesis and reaction conditions. The reasons for such a big difference in the reactivity are unclear, assuming that the surface oxidation state and  $\text{Fe}^0$  content were similar because they were synthesized under the exact same conditions using excess  $\text{NaBH}_4$ . It is unclear if different Fe precursors will affect the nucleation process, crystalline structure, and other properties (e.g., electron transfer, S content, and hydrophobicity) of NZVI or SNZVI, and how these properties affect the reactivity.

Several studies on NZVI or SNZVI using different precursors reported widely divergent reactivity, which is in need of clarification. In this work, NZVI and SNZVI with different Fe precursors ( $\text{Fe}^{3+}$  and  $\text{Fe}^{2+}$ ) and S precursors ( $\text{S}_2\text{O}_4^{2-}$ ,  $\text{S}^{2-}$ , and  $\text{S}_6^{2-}$ ) were synthesized and characterized to determine how different Fe and S precursors influence the physicochemical properties of NZVI or SNZVI (crystalline structure, S amount/distribution/speciation, hydrophobicity, and electron-transfer resistance) and their reactivity with water and a groundwater contaminant (TCE). This understanding helps to resolve apparent discrepancies in the reported reactivity and provides the knowledge to guide (i.e., selecting the precursors) the synthesis of SNZVI with the desired properties and reactivity.

## 2. EXPERIMENTAL SECTION

**2.1. Materials.**  $\text{FeSO}_4 \cdot 7\text{H}_2\text{O}$  (98%),  $\text{FeCl}_2 \cdot 4\text{H}_2\text{O}$  (98%)  $\text{NaBH}_4$  (98%),  $\text{Na}_2\text{S}$  (90%), and TCE ( $\geq 99.5\%$ ) were purchased from Fisher Scientific.  $\text{FeCl}_3$  (97%) and potassium polysulfide ( $\geq 42\%$   $\text{K}_2\text{S}$  basis, which is close to  $\text{K}_2\text{S}_6$ ) were obtained from Sigma-Aldrich.  $\text{Na}_2\text{S}_2\text{O}_4$  ( $\geq 88\%$ ) was obtained from Sinopharm Chemical Reagent Co., Ltd., China. The measured trace metals in the precursor chemicals and the resulting NZVI and SNZVI materials are shown in Figure S2. Deoxygenated deionized water was used in all experiments.

**2.2. Synthesis of NZVI and SNZVI.** The NZVI and SNZVI particles were synthesized according to the previously reported methods.<sup>1,13,19,21,48,49</sup> Briefly, the NZVI particles with

different Fe precursors were synthesized by dropwise addition ( $\sim 7 \text{ mL min}^{-1}$ ) of 200 mL of  $34 \text{ g L}^{-1}$   $\text{NaBH}_4$  solution into a continuously stirred (600 rpm) 200 mL vessel containing  $10 \text{ g L}^{-1}$   $\text{Fe}^{2+}$  or  $\text{Fe}^{3+}$  solution under  $\text{N}_2$  purging, followed by 10 min of stirring. The SNZVI particles with different Fe or S precursors were synthesized by dropwise addition of 200 mL of  $34 \text{ g L}^{-1}$   $\text{NaBH}_4$  and  $2.2 \text{ g L}^{-1}$   $\text{Na}_2\text{S}_2\text{O}_4$  (or  $2.0 \text{ g L}^{-1}$   $\text{Na}_2\text{S}$  or  $1.1 \text{ g L}^{-1}$   $\text{K}_2\text{S}_6$ ) solution into 200 mL of a  $10 \text{ g L}^{-1}$   $\text{Fe}^{2+}$  or  $\text{Fe}^{3+}$  solution while mixing under nitrogen purging. In all cases of SNZVI, the solution volumes and concentrations theoretically provide a 0.14 S/Fe molar ratio. The resulting NZVI or SNZVI suspensions were washed three times with deoxygenated DI water and then dried in a vacuum oven at  $60^\circ\text{C}$  for 8 h. The vacuum was slowly released by air over 3 h to stabilize the particles, which were subsequently ground and stored in sealed vials in an anaerobic glovebox prior to use.

**2.3. Batch Experiments.** Batch reactivity studies were conducted in 160 mL serum bottles containing 100 mL of deoxygenated DI water (pH  $\sim 5.0$ ) or TCE solution and 60 mL of headspace. The bottles were capped by Teflon Mininert valves. In all experiments, the bottles were rotated on an end-over-end rotator at 30 rpm at  $25 \pm 2^\circ\text{C}$ . The reactivity of each NZVI and SNZVI ( $1 \text{ g L}^{-1}$ ) with water was determined over 80 days reaction. The reactivity of each NZVI and SNZVI ( $1 \text{ g L}^{-1}$ ) with TCE ( $70 \mu\text{M}$ ) was also determined over 8 days to assess the application potential for remediation of TCE-contaminated groundwater.

**2.4. Analytical Methods.** The  $\text{H}_2$ , TCE, and its main products ( $\text{C}_2\text{H}_2$ ,  $\text{C}_2\text{H}_4$ , and  $\text{C}_2\text{H}_6$ ) in the headspace were quantified using an Agilent 6850 GC-TCD system and an HP 6890 GC-FID system. The detailed methods of GC measurement, calculations of the total amount of TCE and its products in the reactor, calculations of electron selectivity (defined as the fraction of electron equivalents from  $\text{Fe}^0$  that is used for TCE) have been described in our previous studies.<sup>19,50</sup> The  $\text{Fe}^0$  content in the particles was determined by measuring the  $\text{H}_2$  in the headspace after acidification assay using a 37% HCl solution ( $\text{Fe}^0 + 2\text{H}^+ \rightarrow \text{Fe}^{2+} + \text{H}_2(\text{g})$ ). The actual S/Fe of each material was determined via the measurement of the total S and Fe by ICP-OES (PerkinElmer Optima 8300DV) after acidification using aqua regia solution.<sup>41</sup> The details of various characteristic techniques, including transmission electron microscopy and energy-dispersive X-ray (TEM-EDX) analysis, surface area, determination of hydrophobicity (measuring the water contact angle of the pellets made from each material), and electrochemical impedance spectroscopy (EIS) analysis, have been described in our previous studies.<sup>19,27</sup> Since cobalt radiation has a much higher sensitivity and yields higher quality diffractograms than copper radiation for iron containing materials,<sup>51</sup> X-ray diffraction (XRD) analysis was carried out on PANalytical X'pert PRO MPD with a cobalt source to make phase identification unambiguous.

The S speciation of SNZVI with different S precursors was determined by examining the X-ray absorption near edge structure (XANES) features at the S K-edge at 2.47 keV. The vacuum-dried samples were grounded in an inert environment and thinly deposited on sulfur-free tape. XANES data were collected on beamline 4-3 (SSRL, SLAC synchrotron) using a Si(111) monochromator, under an inert He atmosphere laminar flux at ambient temperature. The samples and reference standards were prepared, as described earlier.<sup>28</sup> Energy was calibrated at 2472.02 eV for each spectrum by recording the sodium thiosulfate spectra between the samples.

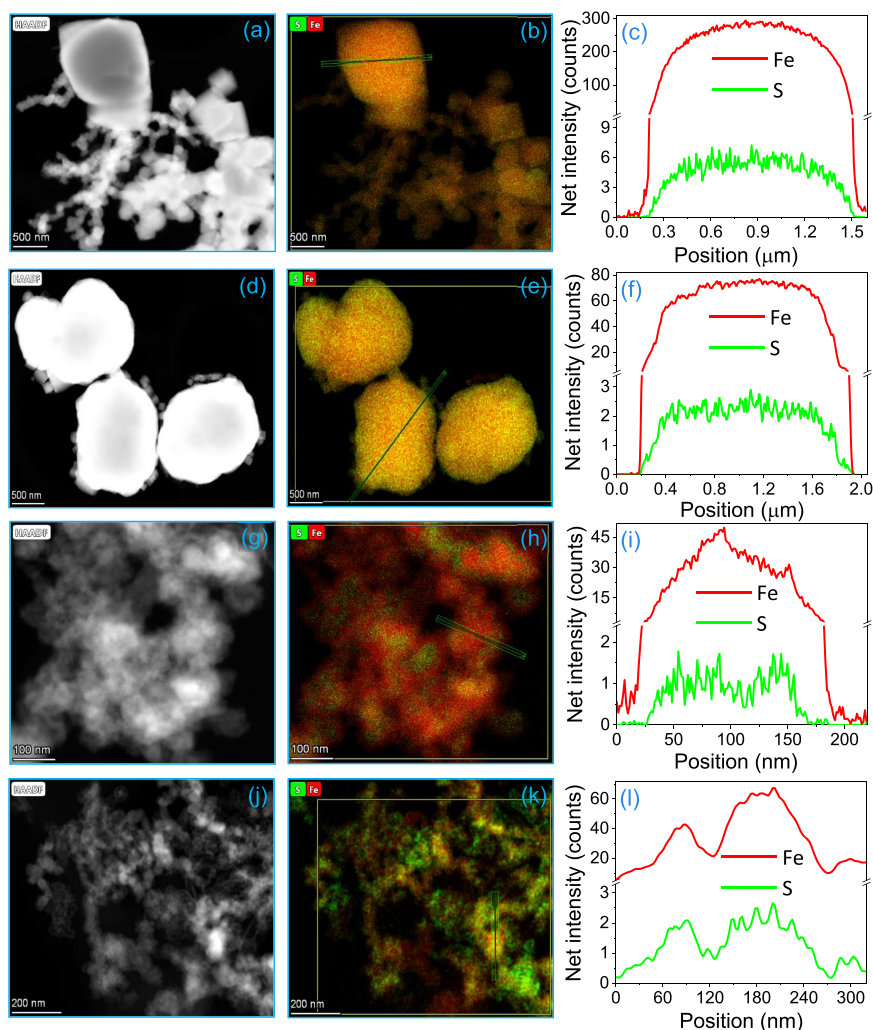


**Figure 1.** High-angle annular dark-field (HAADF) images and elemental distributions of SNZVI made from (a–c)  $\text{Fe}^{2+}$  and  $\text{S}_2\text{O}_4^{2-}$  precursors, (d–f)  $\text{Fe}^{3+}$  and  $\text{S}_2\text{O}_4^{2-}$  precursors, (g–i)  $\text{Fe}^{3+}$  and  $\text{S}^{2-}$  precursors, and (j–l)  $\text{Fe}^{3+}$  and  $\text{S}_6^{2-}$  precursors.

The XANES spectra were recorded using a lytle detector for the samples and a 4-element Si–Li Vortex detector for the references. Self-absorption was considered to be insignificant since the sample mass was  $<10$  mg,<sup>52</sup> and no beam damage was detected in successive scans.

All of the materials used in this paper were prepared and handled identically for experiments and characterizations. We used the experimental protocols to limit the exposure of materials to the air, e.g.,  $\text{N}_2$  purging during the synthesis process, drying the materials in a vacuum oven, grinding–storing–grabbing the materials in an anaerobic glovebox, sealing the materials under a  $\text{N}_2$  atmosphere during transportation to the characterization facilities, and preparing the samples in an anaerobic glovebox on the site for TEM-EDX and XAS measurements. However, some brief exposure to air is inevitable. Specifically, for  $\text{Fe}^0$  content, S content, XRD, and XPS measurements, the samples were exposed to the air for  $\sim 1$  min during the preparation. The results of TEM-EDX, water contact angle, and XPS, XRD, and XAS analyses of NZVI synthesized by  $\text{FeCl}_3$  and SNZVI synthesized by  $\text{FeCl}_3$  and  $\text{Na}_2\text{SO}_4$  were both close to the results from our previous studies,<sup>19,28</sup> suggesting high reproducibility of the synthesis and of the analysis. Regardless, the differences in reactivity relate back to the initial properties of the materials and they do

so in a way that is consistent with expectation based on those properties, as discussed below.

Density functional theory (DFT) calculations were performed to study the impact of the lattice constant on water and H adsorption on the Fe(110) surfaces with or without sulfur incorporation into the Fe body-centered-cubic (BCC) structure. The Fe surfaces were modeled as four-layer,  $(3 \times 3)$ , (110) slabs, with the bottom two layers constrained in bulk positions. The S-in-Fe(110) surfaces were modeled by replacing one surface Fe atom with a S atom. Hydrogen is adsorbed in the hollow sites after DFT optimizations, while the water molecule is adsorbed at the top position of Fe or S. Details of the computational methods are described in our previous study.<sup>28</sup>

### 3. RESULTS AND DISCUSSION

**3.1. Fe and S Precursors Affect the Morphology, Elemental Distribution, S Content, and  $\text{Fe}^0$  Content of NZVI and SNZVI.** Since the  $\text{FeCl}_2$  chemical was not pure (primarily  $\text{FeCl}_2$ , but some yellowing indicated partial oxidation of  $\text{FeCl}_2$  to  $\text{FeCl}_3$ ), we did not include the results of NZVI and SNZVI synthesized by  $\text{FeCl}_2$  into the main discussion. However, the measured crystalline domain size, lattice spacing, lattice constant, electron-transfer resistance, and

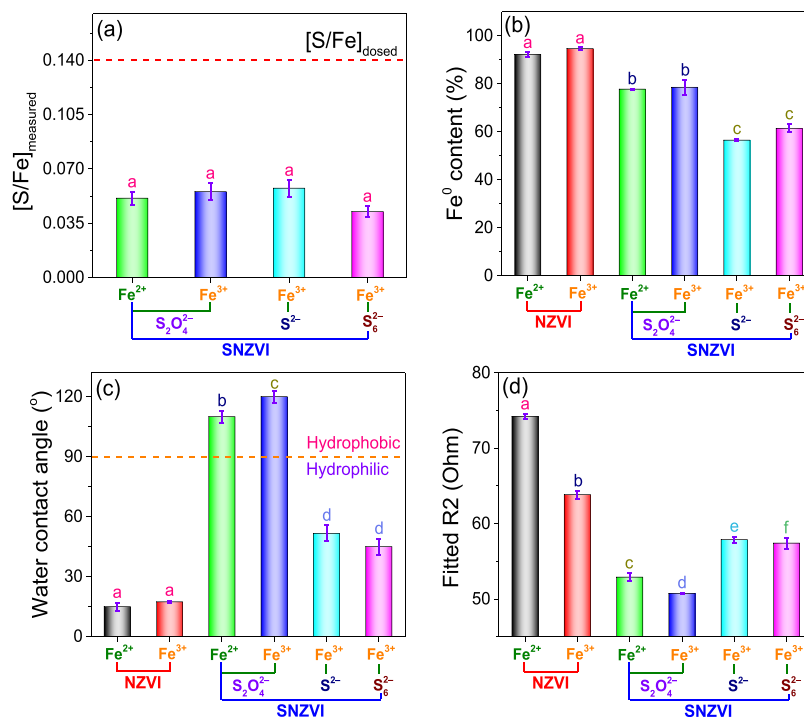


**Figure 2.** (a)  $[S/Fe]_{\text{measured}}$ , (b)  $\text{Fe}^0$  content, (c) water contact angle and of pellets made from NZVI and SNZVI with different Fe or S precursors, and (d) fitted resistance from electrochemical impedance spectroscopy. Different letters indicate significantly different values of the  $\text{Fe}^0$  content,  $[S/Fe]_{\text{measured}}$ , fitted resistance, and water contact angle between NZVI and SNZVI with different Fe and S precursors ( $\alpha = 0.05$ ; one-way analysis of variance (ANOVA)).

the reactivity with TCE for NZVI and SNZVI made from  $\text{FeCl}_2$  (Table S1 and Figure S4) were all between the materials synthesized using  $\text{FeSO}_4$  and  $\text{FeCl}_3$ , but closer to that of the  $\text{FeSO}_4$ . This was consistent with the fact that the  $\text{FeCl}_2$  chemical was likely a mixture of  $\text{FeCl}_2$  and  $\text{FeCl}_3$ , but primarily  $\text{FeCl}_2$ . These results suggest that the anions ( $\text{SO}_4^{2-}$  and  $\text{Cl}^-$ ) do not greatly affect the properties and reactivity of NZVI and SNZVI, which is mainly attributed to the Fe ion precursors. In the following discussion, the  $\text{Fe}^{2+}$  and  $\text{Fe}^{3+}$  represent the  $\text{FeSO}_4$  precursor and  $\text{FeCl}_3$  precursor, respectively.

The initial pH of 10 g L<sup>-1</sup> of  $\text{Fe}^{2+}$  solution and  $\text{Fe}^{3+}$  solution was 3.6 and 1.9, respectively. Particle nucleation and crystal growth are essential steps to obtaining nanoparticles. The black and magnetic particles were observed immediately upon adding a  $\text{NaBH}_4$  solution or a  $\text{NaBH}_4 + \text{Na}_2\text{S}_2\text{O}_4$  solution into the  $\text{Fe}^{2+}$  precursor solution (Figure S3a), indicating that nucleation of  $\text{NZVI}_{\text{Fe}^{2+}}$  and  $\text{SNZVI}_{\text{Fe}^{2+}}$  occurs at the beginning of the synthesis process when pH  $\sim 3.6$ . However, the observation of particles was delayed for the  $\text{Fe}^{3+}$  precursors (Figure S3a,b). The formed particles (likely  $\text{Fe}^0$ ) are dissolved at the lower pH ( $\text{Fe}^0 + 2\text{H}^+ \rightarrow \text{Fe}^{2+} + \text{H}_2$ ) and in the presence of  $\text{Fe}^{3+}$  ( $2\text{Fe}^{3+} + \text{Fe}^0 \rightarrow 3\text{Fe}^{2+}$ ). Observable magnetic particles began to accumulate after  $\sim 2$  min (pH  $\sim 1.5$ ) for the synthesis of  $\text{NZVI}_{\text{Fe}^{3+}}$ , while it took  $\sim 5$  min (pH  $\sim 6.5$ ) for the synthesis of  $\text{SNZVI}_{\text{Fe}^{3+}}$ , consistent with a previous study that investigated the nucleation of  $\text{NZVI}_{\text{Fe}^{3+}}$  and  $\text{SNZVI}_{\text{Fe}^{3+}}$ .<sup>53</sup> In addition to the difference in pH for the initial conditions of the reaction, two other factors may influence the resulting particle properties and reactivity. First, there was  $\text{Fe}^{3+}$  in the solution when  $\text{NZVI}_{\text{Fe}^{3+}}$  or  $\text{SNZVI}_{\text{Fe}^{3+}}$  began to nucleate.<sup>53</sup> This is not the case for the use of  $\text{Fe}^{2+}$  as a precursor. Second, the replacement of a water molecule from the first coordination

shell represents an important step in complex-formation reactions of metal cations and in many redox processes. The water exchange rate of  $[\text{Fe}(\text{H}_2\text{O})_6]^{2+}$  ( $4.4 \times 10^6 \text{ s}^{-1}$ ) is much faster than for  $[\text{Fe}(\text{H}_2\text{O})_6]^{3+}$  ( $1.6 \times 10^2 \text{ s}^{-1}$ ),<sup>54</sup> so the nucleation of  $\text{Fe}^{2+}$  may be faster than  $\text{Fe}^{3+}$ . While complicated, the synthesis procedures used here resulted in materials with very different reactivity, as discussed later.

Both iron precursors ( $\text{Fe}^{2+}$  and  $\text{Fe}^{3+}$ ) resulted in the same typical chain-like structures and comparable elemental distributions of the  $\text{NaBH}_4$ -reduced NZVI particles (Figures S5 and S6), indicating that the differences in reactivity between  $\text{NZVI}_{\text{Fe}^{2+}}$  and  $\text{NZVI}_{\text{Fe}^{3+}}$  discussed later were not related to differences in the morphology or the elemental distribution. Sulfur was clearly identified on the EDX spectra after the sulfidation of NZVI, regardless of the sulfur precursor used (Figures S7–S10). NZVI sulfidation by dithionite resulted in larger particles as compared with the unsulfidized NZVI particles (Figure 1a,d). Both the elemental distribution maps and the intensity profiles across both the smaller and larger individual particles revealed an even distribution of S and Fe in the SNZVI particles synthesized from the  $\text{S}_2\text{O}_4^{2-}$  precursor (Figures 1b,c,e,f, and S11), regardless of the valence state of the Fe precursor. This suggests that these two particle types were similar. In contrast, the SNZVI particles made from the sulfide or polysulfide were much smaller, and their morphology and elemental distribution were different from NZVI and SNZVI made from the  $\text{S}_2\text{O}_4^{2-}$  precursor (Figure 1g–l). These HAADF images and elemental maps suggest that the S precursors, and the different reactivity of the S precursors with Fe, resulted in differences in the morphology and elemental distribution of SNZVI, which would also affect the S speciation and crystallinity of the SNZVI particles, as discussed later. The differences in the primary particle size also led to a different

N<sub>2</sub>-Brunauer–Emmett–Teller (BET) specific surface area (Figure S12).

The measured S/Fe molar ratio ( $[\text{S}/\text{Fe}]_{\text{measured}}$ ) in the particles was  $\sim 0.05$  using a dose of 0.14 S/Fe molar ratio in the synthesis (Figure 2a), indicating that the Fe and S precursors did not vary the S/Fe ratio. The amount of incorporated S was therefore not considered in the following discussion of the impacts of the Fe and S precursors. No S or  $\text{SO}_4^{2-}$  was detected by the XPS analysis of  $\text{NZVI}_{\text{Fe}^{2+}}$  and  $\text{NZVI}_{\text{Fe}^{3+}}$  (Figure S13), suggesting that there is no sulfur in the NZVI structures, i.e., the  $\text{SO}_4^{2-}$  precursor was not reduced to sulfides or adsorbed to the surface, and there is no S contamination from the chemicals besides the S precursors. The S 2p narrow spectra of SNZVI were also quite similar. These results indicate that the contributions of shell differences to the reactivity are likely less important than the differences in the Fe<sup>0</sup> core.

The Fe<sup>0</sup> content of the particles (Figure 2b) represents their potential to degrade contaminants through chemical reduction. The Fe<sup>0</sup> content of NZVI with the Fe<sup>2+</sup> precursor ( $\sim 92\%$ ) was close to that of NZVI with the Fe<sup>3+</sup> precursor ( $\sim 95\%$ ), suggesting that the Fe precursor did not affect the Fe<sup>0</sup> content of NZVI that was synthesized using excess reductant ( $\text{NaBH}_4$ ). The Fe<sup>0</sup> content of SNZVI ( $\sim 78\%$ ) made using dithionite was slightly lower than that of NZVI due to the incorporation of S.<sup>29</sup> The Fe precursor did not affect the Fe<sup>0</sup> content of SNZVI. However, using sulfide or polysulfide as a sulfur source led to SNZVI with statistically significantly lower amounts of Fe<sup>0</sup>, suggesting that the choice of sulfur species used in the synthesis affected the Fe<sup>0</sup> content of the resulting particles. This lower Fe<sup>0</sup> content is consistent with the differences in sulfur speciation in the particles, considering that there is a similar amount of S in the materials (Figure 1a). More Fe is present as FeS in SNZVI synthesized with the S<sup>2-</sup> and S<sub>6</sub><sup>2-</sup> precursors (as shown by the S K-edge XANES spectra in Figure 3 below) than for SNZVI made using S<sub>2</sub>O<sub>4</sub><sup>2-</sup> as a

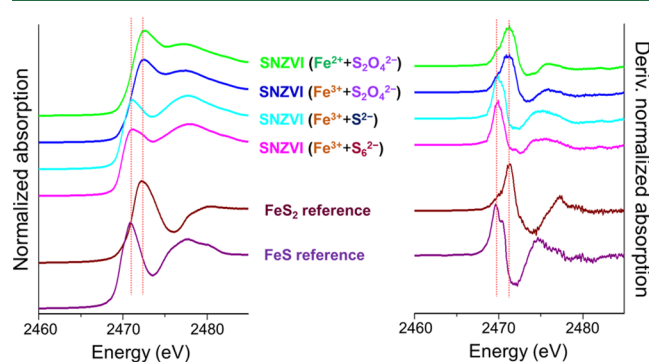


**Figure 3.** S K-edge XANES of SNZVI synthesized using different Fe and S precursors and their derivative spectra in comparison to pyrite ( $\text{FeS}_2$ ) and mackinawite ( $\text{FeS}$ ) reference samples features.

precursor, where the Fe species are mainly  $\text{FeS}_2$ . In addition, there is an iron oxide (maghemite,  $\text{Fe}_2\text{O}_3$ ) peak observed in the XRD patterns of SNZVI with the S<sup>2-</sup> and S<sub>6</sub><sup>2-</sup> precursors (Figure S14e,f). This observation is consistent with the lower Fe<sup>0</sup> content of these two materials than other materials without iron oxide peaks in the XRD patterns (present as amorphous phase and/or below the detection limit of XRD,  $\sim 5$  wt %).

**3.2. S Precursors Control S speciation, while Fe Precursors Alter Crystalline Structure.** XANES analysis at

the S K-edge was performed to determine if the Fe and S precursors affected the S speciation in the resulting SNZVI. The dotted lines in Figure 3 show the positions of the S K-edge XANES spectra for the iron monosulfide ( $\text{FeS}$ ) structure at 2470.9 eV and iron disulfide ( $\text{FeS}_2$ ) structure at 2472.3 eV.<sup>55,56</sup>  $\text{FeS}_2$  was the main S species of SNZVI prepared by S<sub>2</sub>O<sub>4</sub><sup>2-</sup> regardless of the Fe<sup>2+</sup> or Fe<sup>3+</sup> precursor, and the XANES spectra contained very minor (or no) contribution of FeS features. In contrast, FeS was the major S species of SNZVI prepared by S<sup>2-</sup> or S<sub>6</sub><sup>2-</sup>. This indicates that the S speciation in synthesized SNZVI can be controlled by the S precursors used, since the S content in these materials was quite close, as shown in Figure 1a. While a previous study suggested that the amount of S incorporated into the Fe<sup>0</sup> BCC structure affects the S speciation,<sup>28</sup> the results of this study indicate that altering the S precursor allows tuning the S speciation in SNZVI.

These S speciation results are consistent with the water contact angle (hydrophobicity) of the resulting particles (Figure 2c). The water contact angles of NZVI with Fe<sup>2+</sup> or Fe<sup>3+</sup> precursors were  $\sim 15^\circ$ , suggesting that the Fe precursors did not significantly affect the hydrophobicity of NZVI. After the co-sulfidation with S<sub>2</sub>O<sub>4</sub><sup>2-</sup>, the hydrophobicity of SNZVI was greatly increased ( $>100^\circ$ ). However, the water contact angle of SNZVI with the S<sup>2-</sup> and S<sub>6</sub><sup>2-</sup> precursors (mainly FeS) was only  $\sim 50$  and  $45^\circ$ , respectively, which was much lower than that of SNZVI with the S<sub>2</sub>O<sub>4</sub><sup>2-</sup> precursor (mainly  $\text{FeS}_2$ ). This was consistent with reported DFT calculations that sulfur makes the Fe surfaces more hydrophobic and pyrite is more hydrophobic than mackinawite.<sup>28,57</sup>

We also compared the effect of the Fe precursor on the resulting crystalline properties of NZVI and SNZVI. Different intensities and positions of the Fe peaks were observed in the XRD patterns (Figure S14); profile fitting and refinement (Rietveld) (Figure S15) were carried out to obtain precise values of the lattice constant ( $a$ ), crystalline domain size ( $D$ ), and lattice spacing ( $d$ ) (Figure S16).<sup>58</sup> Specifically, the Fe(110) peak observed for  $\text{NZVI}_{\text{Fe}^{3+}}$  has a lower intensity and is shifted compared to the spectra of  $\text{NZVI}_{\text{Fe}^{2+}}$  (Figure 4a). Generally, the lower/broader peak is attributed to either the smaller domain size or to poorer crystallinity. Since the crystalline domain size ( $D$ ) of the Fe(110) plane of  $\text{NZVI}_{\text{Fe}^{3+}}$  was similar to that of  $\text{NZVI}_{\text{Fe}^{2+}}$  (Figure S16a), the higher intensity of  $\text{NZVI}_{\text{Fe}^{2+}}$  indicates that it was more crystalline than  $\text{NZVI}_{\text{Fe}^{3+}}$ . The lattice spacing ( $d$ ) and lattice constant ( $a$ ) of the Fe(110) plane of  $\text{NZVI}_{\text{Fe}^{3+}}$  were larger than those of  $\text{NZVI}_{\text{Fe}^{2+}}$  (Figure S16d). A similar shift was observed between the Fe(110) peaks of SNZVI with the Fe<sup>2+</sup> and Fe<sup>3+</sup> precursors (Figure 4b). The higher peak intensity and  $D$  values of SNZVI than those of NZVI indicate that sulfidation improved the crystallinity and had a higher impact on the crystallinity than the Fe precursor. For different S precursors, there is a slight shift between SNZVI with the S<sub>6</sub><sup>2-</sup> and S<sup>2-</sup> precursors, while a larger shift and a more intense peak were observed for the SNZVI with the S<sub>2</sub>O<sub>4</sub><sup>2-</sup> precursor (Figure 4c). Similar results were observed for Fe(200) and Fe(211) planes (Figure S14c,d). The choice of the sulfur precursors caused more pronounced shifts than that of the Fe precursors, indicating that the BCC lattice structure of Fe<sup>0</sup> was distorted, especially when dithionite is used.<sup>28</sup> This is probably because new phases (i.e., FeS or  $\text{FeS}_2$ ) were formed as suggested by the S K-edge XANES results (Figure 3). The distorted lattice constants (larger lattice constant tends to facilitate the electron transfer)

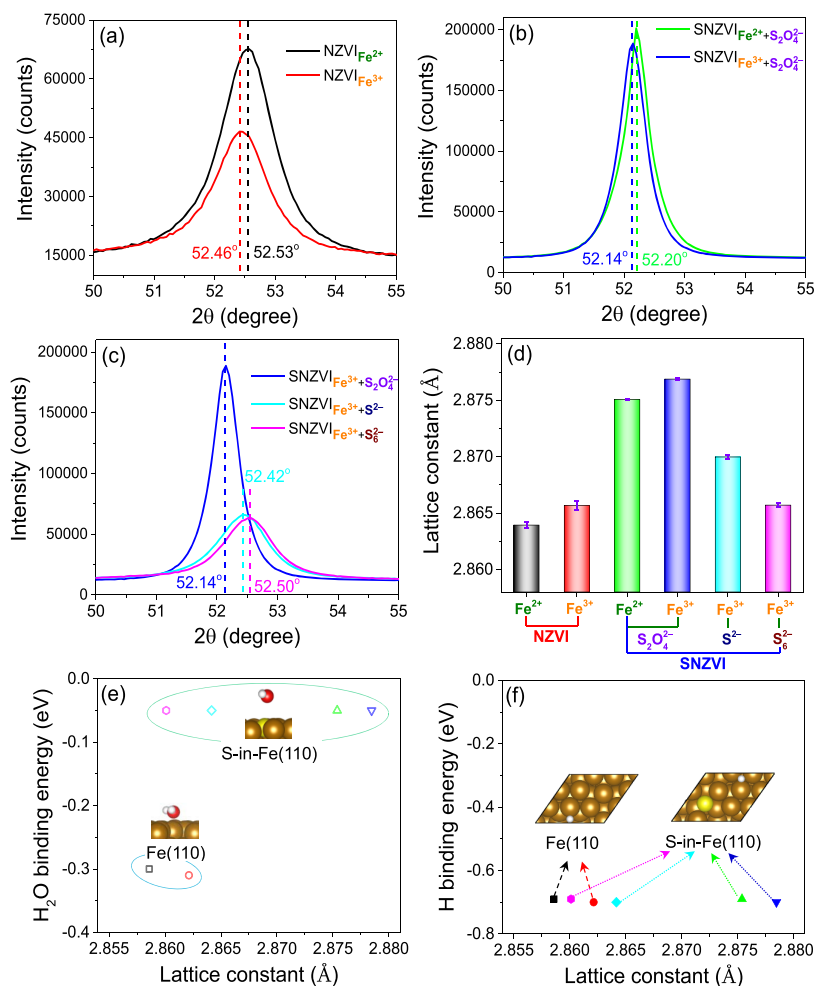


**Figure 4.** XRD patterns of Fe(110) of (a) NZVI and (b) SNZVI made from different Fe precursors and (c) SNZVI made from different S precursors. (d) Lattice constants of the Fe BCC structure according to the XRD Rietveld refinement. Different letters indicate significantly different values of the lattice constant between NZVI and SNZVI with different Fe and S precursors ( $\alpha = 0.05$ ; one-way ANOVA). Impact of the lattice constant on the DFT-calculated (e)  $\text{H}_2\text{O}$  and (f) H binding energies at Fe(110) and S-doped Fe(110) surfaces. The insets show the  $\text{H}_2\text{O}$  and H adsorption geometries after DFT structural relaxations.

and the presence of iron sulfides would significantly alter the electron-transfer resistance due to the lower band gap of iron sulfides compared to iron oxides ( $\text{Fe}_2\text{O}_3$ ), which is consistent with the measurements of electron-transfer resistance (Figure 2d).

Note that there was no shift between the XRD patterns of the SNZVI used in this study and SNZVI that had been synthesized and analyzed five months prior with the same Fe and S precursors (Figure S17a,b). This indicates good reproducibility of the XRD analysis and indicates that the shifts observed in this study were from the samples and not from the instrument. The values of the shift in  $2\theta$  from  $\text{Fe}^{3+}$  to  $\text{Fe}^{2+}$  increased with increasing of  $2\theta$  (Figure S17c), which also indicates that the shifts were from the samples. In addition, the XRD analysis was performed immediately after the instrument calibration, which also limits the impact of instrument conditions on the  $2\theta$  values of the Fe peaks. The average lattice constants of the (110), (200), and (211) planes of NZVI and SNZVI with the  $\text{Fe}^{3+}$  precursor were significantly larger than those with the  $\text{Fe}^{2+}$  precursor, respectively, and the average lattice constant of SNZVI made from the  $\text{S}_2\text{O}_4^{2-}$  precursor was significantly larger than that with the  $\text{S}^{2-}$  or  $\text{S}_6^{2-}$  precursor (Figure 4d). These results indicate that the choice of

the Fe and S precursors affect the crystalline structure, including the crystallinity, crystalline domain size, lattice spacing, and lattice constant, which would further affect their physicochemical and reactive properties, e.g., electron transfer.

The charge-transfer resistance of NZVI and SNZVI with different precursors was probed by electrochemical impedance spectroscopy (EIS) (Figure S18). Since all samples were pelleted with the same pressure ( $\sim 5$  tons) and weight ( $\sim 40$  mg), it is assumed that the contact resistance between the pellet and Ti mesh is similar, and the differences in the fitted resistance (R2) from the EIS results reflect their differences in the electron-transfer resistance. The fitted R2 of NZVI $_{\text{Fe}^{3+}}$  was lower than that of NZVI $_{\text{Fe}^{2+}}$  (Figure 2d), suggesting its lower resistance to electron transfer. The NZVI $_{\text{Fe}^{2+}}$  had a smaller lattice constant, that is, the smaller interatomic distance, and the valence electrons require more energy to be released upon oxidation. As a rule of thumb, the band energy gap is inversely proportional to the interatomic distance.<sup>60,61</sup> Thus, the NZVI $_{\text{Fe}^{3+}}$  and SNZVI $_{\text{Fe}^{3+}}$  with larger lattice constants (Figure 4d) had a lower resistance to electron transfer than NZVI $_{\text{Fe}^{2+}}$  and SNZVI $_{\text{Fe}^{2+}}$ , respectively (Figure 2d). In addition, the electron-transfer resistance of SNZVI synthesized by  $\text{S}^{2-}$  and  $\text{S}_6^{2-}$  was higher than those made by the  $\text{S}_2\text{O}_4^{2-}$  precursor.

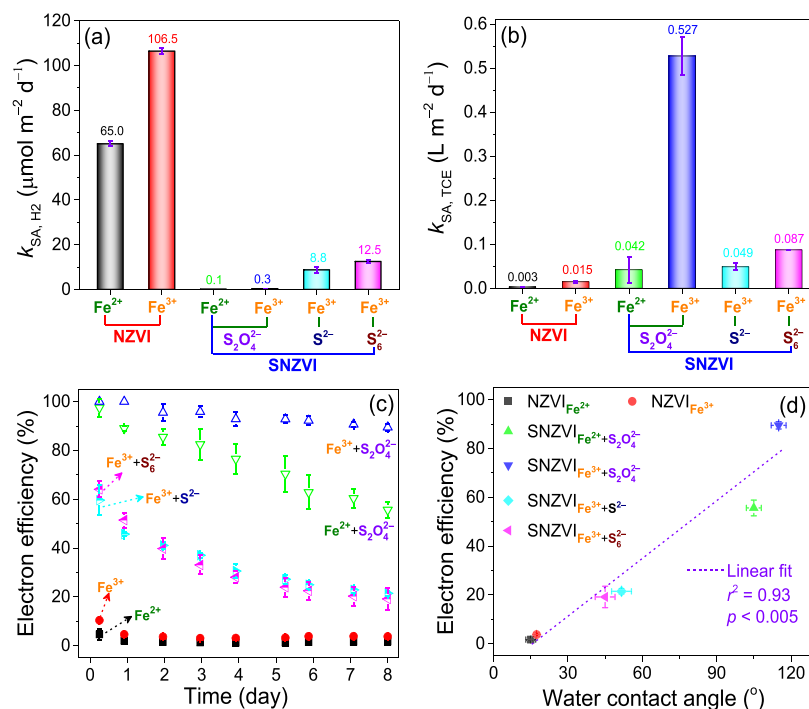


**Figure 5.** Impact of different Fe and S precursors on the reactivity of NZVI and SNZVI with water and TCE. (a)  $k_{SA,H_2}$  without TCE (calculated from the first 8 days of reaction); (b)  $k_{SA,TCE}$ ; (c) electron efficiency for TCE degradation as a function of reaction time; (d) correlation between electron efficiency and hydrophobicity. Linear correlation lines with  $r^2$  and  $p$  values were calculated using R (initial pH = 5.0,  $T = 25 \pm 2$  °C, initial TCE = 70  $\mu\text{M}$ , NZVI or SNZVI = 1.0 g  $\text{L}^{-1}$ ).

Besides the lattice constant, the higher resistance of SNZVI made by the  $\text{S}^{2-}$  or  $\text{S}_6^{2-}$  precursors was also consistent with their lower  $\text{Fe}^0$  (conductive metal) content (Figure 2b) and higher  $\text{Fe}_2\text{O}_3$  (insulator) content (Figure S14e,f). The  $\text{Fe}_2\text{O}_3$  with a high band gap (2.20 eV) was expected to have a higher resistance than  $\text{Fe}^0$  (0.00 eV),  $\text{FeS}$  (0.10 eV), and  $\text{FeS}_2$  (0.95 eV).<sup>45</sup> Alloying oxygen with iron sulfides would also increase the band gap of  $\text{FeS}$ , increasing the resistance for electron transfer.<sup>45,59</sup>

The impact of the lattice constant of NZVI and SNZVI on their affinity toward  $\text{H}_2\text{O}$  (Figure 4e) and  $\text{H}$  (Figure 4f) was further investigated by DFT calculations. The lattice constants do not significantly affect the binding energies of  $\text{H}_2\text{O}$  onto the surface for NZVI and SNZVI, respectively (Figure 4e). Regardless of the lattice constant, the bindings of  $\text{H}_2\text{O}$  onto the SNZVI surfaces are much weaker (i.e., more positive) than those onto the NZVI surfaces. Note that S significantly hinders the H adsorption, and H migrates from the S to the Fe site upon optimization. The varied lattice constants of NZVI and SNZVI do not significantly affect the binding energies of H (Figure 4f) onto their Fe surfaces after DFT structural relaxations. These results suggest that the impact of the lattice constant on the hydrophobicity of SNZVI could be ruled out, and the S speciation controls the hydrophobicity of SNZVI.

**3.3. Fe and S Precursors Affect the Corrosion of NZVI and SNZVI by Water.** The Fe and S precursors resulted in differences in the reactivity of NZVI and SNZVI with water (without TCE), according to the  $\text{H}_2$  evolution measured during their aging in water over 80 days (Figure S19). For comparison, the initial rates of  $\text{H}_2$  evolution (first 8 days) for different NZVI and SNZVI in water (without TCE) were described as a surface-area-normalized zero-order rate constant (Figure 5a). The  $k_{SA,H_2}$  of NZVI $_{\text{Fe}^{3+}}$  was approximately two

times higher than that of NZVI $_{\text{Fe}^{2+}}$ , although their  $\text{Fe}^0$  content (Figure 2b), hydrophobicity (Figure 2c), oxidation state, and morphology (Figures S5 and S6) were quite similar. This is consistent with the increased lattice constant (Figure 4d) and decreased charge-transfer resistance (Figure 2d) of NZVI $_{\text{Fe}^{3+}}$  as compared with NZVI $_{\text{Fe}^{2+}}$ , promoting the electron transfer from  $\text{Fe}^0$  to water. For similar reasons, the  $\text{H}_2$  evolution by SNZVI $_{\text{Fe}^{3+}}$  was approximately three times faster than that by SNZVI $_{\text{Fe}^{2+}}$ . Sulfidation of NZVI greatly inhibited the  $\text{H}_2$  evolution as expected,<sup>19,20</sup> and almost no  $\text{H}_2$  was detected by SNZVI with the  $\text{S}_2\text{O}_4^{2-}$  precursor within the initial 4 days (Figure S19a), probably aided by the high hydrophobicity (Figure 2c).

The S precursors ( $\text{S}_2\text{O}_4^{2-}$ ,  $\text{S}^{2-}$ , and  $\text{S}_6^{2-}$ ) also greatly affected the reactivity of SNZVI ( $\text{Fe}^{3+}$  precursor) with water (Figure 5a). The  $k_{SA,H_2}$  of SNZVI with the  $\text{S}^{2-}$  and  $\text{S}_6^{2-}$  precursors was  $\sim 30$  and  $\sim 40$  times higher than that with  $\text{S}_2\text{O}_4^{2-}$ , respectively, though their S contents were similar (Figure 2a) and the charge-transfer resistances of SNZVI made from the  $\text{S}^{2-}$  and  $\text{S}_6^{2-}$  precursors were higher than that made from  $\text{S}_2\text{O}_4^{2-}$  (Figure 2d). This is because the SNZVI with the  $\text{S}^{2-}$  or  $\text{S}_6^{2-}$  precursors was hydrophilic, while the SNZVI with the  $\text{S}_2\text{O}_4^{2-}$  precursor was hydrophobic (Figure 2c). Iron monosulfide ( $\text{FeS}$ ) as the main species of the SNZVI with the  $\text{S}^{2-}$  or  $\text{S}_6^{2-}$  precursors (Figure 3) is more favorable to water adsorption and to H adsorption than iron disulfide ( $\text{FeS}_2$ ), the main species of the SNZVI made from the  $\text{S}_2\text{O}_4^{2-}$  precursor.<sup>28</sup> Interestingly, the accumulated  $\text{H}_2$  (%) by SNZVI made using the  $\text{S}^{2-}$  or  $\text{S}_6^{2-}$  precursors was close to that of NZVI made using the  $\text{Fe}^{2+}$  precursor (Figure S19b). Thus, it cannot be generalized that all SNZVI is less reactive with water than NZVI. Rather, the reactivity with water depends on the specific physicochemical properties of materials of the resulting

materials (e.g., hydrophobicity, S speciation, charger transfer), which is affected by the Fe and S precursors used for the synthesis.

**3.4. Fe and S Precursors Affect the Reactivity and Selectivity of NZVI and SNZVI With TCE.** The reactivity of NZVI and SNZVI with different Fe and S precursors for TCE was evaluated (Figure S20). The choice of the Fe and S precursor did not change the degradation products from TCE reduction by NZVI or SNZVI. However, both the Fe and S precursors affected the reaction rate of TCE with NZVI or SNZVI. The surface area-normalized first-order kinetic rate constant of TCE removal ( $k_{SA,TCE}$ ) by NZVI or SNZVI made from the  $Fe^{3+}$  precursor was  $\sim 5$  and 13 times higher than the  $Fe^{2+}$  precursor, respectively (Figure 5b), and the  $k_{SA,TCE}$  of SNZVI using the  $S_2O_4^{2-}$  precursor was  $\sim 11$ -fold and 6-fold higher than that using the  $S^{2-}$  or  $S_6^{2-}$  precursors (Figure 5b), respectively. These results were consistent with the expanded lattice (lower energy gap) (Figure 4d), lower charge-transfer resistance (facilitated electron transfer) (Figure 2d), and higher hydrophobicity (Figure 2c) of the materials using the  $Fe^{3+}$  and  $S_2O_4^{2-}$  precursors compared to the other precursors. In addition, the higher reactivity of  $SNZVI_{Fe^{3+}}$  than  $SNZVI_{Fe^{2+}}$  with similar  $[S/Fe]_{measured}$  also appears to be true for the  $S^{2-}$  precursor. The  $k_{SA,TCE}$  ( $0.049\text{ L m}^{-2}\text{ d}^{-1}$ ) by the SNZVI synthesized by the  $Fe^{3+}$  and  $S^{2-}$  precursors in this work was  $\sim 3.6$ – $5.5$  times higher than those ( $\sim 0.009$ – $0.015\text{ L m}^{-2}\text{ d}^{-1}$ ) in a previous study,<sup>41</sup> where the SNZVI was synthesized by the  $Fe^{2+}$  and  $S^{2-}$  precursors when the  $[S/Fe]_{measured}$  (0.035 or 0.05) was similar to this study.

The electron efficiency of TCE degradation by NZVI or SNZVI made from different precursors as a function of the reaction time is shown in Figure 5c. For all of the materials, the electron efficiency gradually decreased as the reaction proceeded. This is because the concentration of TCE decreases and the fraction of electrons from Fe oxidation going to TCE decreases relative to the stable reaction with water (Figure S21).<sup>26</sup> Since SNZVI cannot activate and use the  $H_2$  for TCE reduction,<sup>18</sup> the increasing discrepancy between the electrons for  $H_2$  evolution and TCE reduction resulted in the decreasing electron efficiency. Therefore, the electron efficiency would be affected by the ratio of Fe/TCE, as was previously shown for NZVI and SNZVI.<sup>27,50</sup> These data suggest that using the  $Fe^{3+}$  and  $S_2O_4^{2-}$  precursors to synthesize NZVI or SNZVI (for 0.05  $[S/Fe]_{measured}$  materials) rather than other precursors would reduce the amount of NZVI or SNZVI material required and provide greater reactivity with TCE.

The electron efficiency of the materials for TCE degradation after 8 days of reaction tended to positively correlate with the hydrophobicity ( $r^2 = 0.93$ ,  $p < 0.01$ ) (Figure 5d), no matter what Fe and S precursor was used. Note that the correlation between electron efficiency and hydrophobicity was maintained during the reaction ( $r^2 > 0.88$ ,  $p < 0.005$ ) (Figure S22), despite having the electron efficiency decrease over time. These results suggest that tuning the hydrophobicity of SNZVI via different S precursors may allow maximizing the electron efficiency for TCE degradation. This correlation also suggests that the electron efficiency of the more hydrophilic SNZVI is mainly attributed to the inhibition of  $H_2$  evolution, while for the more hydrophobic SNZVI, other factors (e.g., electron transfer or TCE reactivity) further determine the electron efficiency for TCE degradation since the  $H_2$  evolution is already largely inhibited.

## 4. ENVIRONMENTAL IMPLICATIONS

The results of this study indicate that different Fe and S precursors can affect the physicochemical properties of NZVI and SNZVI, including the crystalline structure, lattice constant, charge-transfer resistance, hydrophobicity, and S speciation, which largely determine the reactivity and selectivity of NZVI and SNZVI. The information on these properties will allow better comparisons and prediction of the reactivity/selectivity of NZVI and SNZVI with the same or different precursors. The Fe precursors can affect the lattice constant of Fe body-centered cubic structure and result in varied electron transfer, while the S precursors can control the S speciation ( $FeS$  vs  $FeS_2$ ) in SNZVI and result in varied hydrophobicity. As an important index of a remediation agent, the electron efficiency of SNZVI is strongly correlated with the hydrophobicity of SNZVI. The results of electron efficiency evaluations suggest that tuning the physicochemical properties of SNZVI by selecting appropriate precursors can be a feasible way to improve the reactivity and selectivity for the reduction of contaminants over the reduction of water. Besides improving our understanding of the batch-to-batch reactivities of synthesized SNZVI in different labs, these findings can also guide the rational synthesis of commercial ZVI, NZVI, and SNZVI particles (e.g., selecting appropriate precursors) and benefit the investigation of these commercial particles' reactivity for environmental remediation.

## ■ ASSOCIATED CONTENT

### Supporting Information

The Supporting Information is available free of charge at <https://pubs.acs.org/doi/10.1021/acs.est.0c03879>.

Dechlorination rate of antibiotic florfenicol by NZVI and SNZVI with  $Fe^{2+}$  or  $Fe^{3+}$  precursors, properties and reactivity of NZVI and SNZVI made from  $FeCl_2$ , TEM images and elemental distribution of NZVI and SNZVI; surface area, XRD patterns and Rietveld refinement, XPS analysis, EIS analysis, accumulated  $H_2$  with or without TCE, TCE and its main degradation products of NZVI and SNZVI with different precursors (PDF)

## ■ AUTHOR INFORMATION

### Corresponding Author

Gregory V. Lowry – Department of Civil and Environmental Engineering and Center for Environmental Implications of NanoTechnology, Carnegie Mellon University, Pittsburgh, Pennsylvania 15213, United States; [orcid.org/0000-0001-8599-008X](https://orcid.org/0000-0001-8599-008X); Phone: (412) 268-2948; Email: [glowry@cmu.edu](mailto:glowry@cmu.edu); Fax: (412) 268-7813

### Authors

Jiang Xu – Department of Civil and Environmental Engineering and Center for Environmental Implications of NanoTechnology, Carnegie Mellon University, Pittsburgh, Pennsylvania 15213, United States; [orcid.org/0000-0003-0369-4848](https://orcid.org/0000-0003-0369-4848)

Astrid Avellan – Department of Civil and Environmental Engineering and Center for Environmental Implications of NanoTechnology, Carnegie Mellon University, Pittsburgh, Pennsylvania 15213, United States; [orcid.org/0000-0001-6081-4389](https://orcid.org/0000-0001-6081-4389)

Hao Li – Department of Chemistry and the Oden Institute for Computational Engineering and Sciences, The University of Texas at Austin, Austin, Texas 78712, United States

Elizabeth A. Clark – Department of Materials Science and Engineering, Carnegie Mellon University, Pittsburgh, Pennsylvania 15213, United States

Graeme Henkelman – Department of Chemistry and the Oden Institute for Computational Engineering and Sciences, The University of Texas at Austin, Austin, Texas 78712, United States; [orcid.org/0000-0002-0336-7153](https://orcid.org/0000-0002-0336-7153)

Ralf Kaegi – Eawag, Swiss Federal Institute of Aquatic Science and Technology, 8600 Dübendorf, Switzerland; [orcid.org/0000-0002-2430-4733](https://orcid.org/0000-0002-2430-4733)

Complete contact information is available at:  
<https://pubs.acs.org/10.1021/acs.est.0c03879>

## Notes

The authors declare no competing financial interest.

## ACKNOWLEDGMENTS

The authors thank Dr. Zimo Lou and Zhen Cao at Zhejiang University for measuring the electrochemical impedance spectroscopy (EIS) and sulfur content of the materials. The authors thank the NSF and EPA funding under NSF Cooperative Agreement EF-1266252, Center for the Environmental Implications of NanoTechnology (CEINT) for partial support. Part of this work has been conducted on beamline 4–1 at the Stanford Synchrotron Radiation Lightsource (SSRL). Use of SSRL, SLAC National Accelerator Laboratory, is supported by the U.S. Department of Energy, Office of Science, Office of Basic Energy Sciences under Contract No. DE-AC02-76SF00515. The contents of this publication are solely the responsibility of the authors and do not necessarily represent the official views of NIGMS or NIH. The authors acknowledge the support of the Scientific Center for Optical and Electron Microscopy ScopeM of the Swiss Federal Institute of Technology ETHZ.

## REFERENCES

- (1) Wang, C.; Zhang, W. Synthesizing Nanoscale Iron Particles for Rapid and Complete Dechlorination of TCE and PCBs. *Environ. Sci. Technol.* **1997**, *31*, 2154–2156.
- (2) Elliott, D. W.; Zhang, W. Field Assessment of Nanoscale Bimetallic Particles for Groundwater Treatment. *Environ. Sci. Technol.* **2001**, *35*, 4922–4926.
- (3) Liu, Y.; Lowry, G. V. Effect of Particle Age ( $\text{Fe}^0$  Content) and Solution pH on NZVI Reactivity:  $\text{H}_2$  Evolution and TCE Dechlorination. *Environ. Sci. Technol.* **2006**, *40*, 6085–6090.
- (4) Liu, X.; Cao, Z.; Yuan, Z.; Zhang, J.; Guo, X.; Yang, Y.; He, F.; Zhao, Y.; Xu, J. Insight Into the Kinetics and Mechanism of Removal of Aqueous Chlorinated Nitroaromatic Antibiotic Chloramphenicol by Nanoscale Zero-Valent Iron. *Chem. Eng. J.* **2018**, *334*, 508–518.
- (5) Xu, J.; Tang, J.; Baig, S. A.; Lv, X.; Xu, X. Enhanced Dechlorination of 2,4-Dichlorophenol by Pd/Fe- $\text{Fe}_3\text{O}_4$  Nanocomposites. *J. Hazard. Mater.* **2013**, *244-245*, 628–636.
- (6) Bleyl, S.; Kopinke, F.; Mackenzie, K. Carbo-Iron—Synthesis and Stabilization of Fe(0)-doped Colloidal Activated Carbon for in Situ Groundwater Treatment. *Chem. Eng. J.* **2012**, *191*, 588–595.
- (7) Xu, J.; Sheng, T.; Hu, Y.; Baig, S. A.; Lv, X.; Xu, X. Adsorption–Dechlorination of 2,4-Dichlorophenol Using Two Specified MWCNTs-stabilized Pd/Fe Nanocomposites. *Chem. Eng. J.* **2013**, *219*, 162–173.
- (8) Ling, L.; Zhang, W. Enrichment and Encapsulation of Uranium with Iron Nanoparticle. *J. Am. Chem. Soc.* **2015**, *137*, 2788–2791.
- (9) Schrick, B.; Blough, J. L.; Jones, A. D.; Mallouk, T. E. Hydrodechlorination of Trichloroethylene to Hydrocarbons Using Bimetallic Nickel-Iron Nanoparticles. *Chem. Mater.* **2002**, *14*, 5140–5147.
- (10) He, F.; Zhao, D. Manipulating the Size and Dispersibility of Zerovalent Iron Nanoparticles by Use of Carboxymethyl Cellulose Stabilizers. *Environ. Sci. Technol.* **2007**, *41*, 6216–6221.
- (11) Hoch, L. B.; Mack, E. J.; Hydutsky, B. W.; Hershman, J. M.; Skluzacek, J. M.; Mallouk, T. E. Carbothermal Synthesis of Carbon-Supported Nanoscale Zero-Valent Iron Particles for the Remediation of Hexavalent Chromium. *Environ. Sci. Technol.* **2008**, *42*, 2600–2605.
- (12) Xu, J.; Liu, X.; Lowry, G. V.; Cao, Z.; Zhao, H.; Zhou, J. L.; Xu, X. Dechlorination Mechanism of 2,4-Dichlorophenol by Magnetic MWCNTs Supported Pd/Fe Nanohybrids: Rapid Adsorption, Gradual Dechlorination, and Desorption of Phenol. *ACS Appl. Mater. Interfaces* **2016**, *8*, 7333–7342.
- (13) Kim, E.; Kim, J.; Azad, A.; Chang, Y. Facile Synthesis and Characterization of Fe/FeS Nanoparticles for Environmental Applications. *ACS Appl. Mater. Interfaces* **2011**, *3*, 1457–1462.
- (14) Rajajayavel, S. R. C.; Ghoshal, S. Enhanced Reductive Dechlorination of Trichloroethylene by Sulfidated Nanoscale Zerovalent Iron. *Water Res.* **2015**, *78*, 144–153.
- (15) Tang, J.; Tang, L.; Feng, H.; Zeng, G.; Dong, H.; Zhang, C.; Huang, B.; Deng, Y.; Wang, J.; Zhou, Y. pH-dependent Degradation of p-Nitrophenol by Sulfidated Nanoscale Zerovalent Iron Under Aerobic or Anoxic Conditions. *J. Hazard. Mater.* **2016**, *320*, 581–590.
- (16) Cao, Z.; Liu, X.; Xu, J.; Zhang, J.; Yang, Y.; Zhou, J.; Xu, X.; Lowry, G. V. Removal of Antibiotic Florfenicol by Sulfide-Modified Nanoscale Zero-Valent Iron. *Environ. Sci. Technol.* **2017**, *51*, 11269–11277.
- (17) Xu, J.; Cao, Z.; Wang, Y.; Zhang, Y.; Gao, X.; Ahmed, M. B.; Zhang, J.; Yang, Y.; Zhou, J. L.; Lowry, G. V. Distributing Sulfidized Nanoscale Zerovalent Iron onto Phosphorus-Functionalized Biochar for Enhanced Removal of Antibiotic Florfenicol. *Chem. Eng. J.* **2019**, *359*, 713–722.
- (18) He, F.; Li, Z.; Shi, S.; Xu, W.; Sheng, H.; Gu, Y.; Jiang, Y.; Xi, B. Dechlorination of Excess Trichloroethene by Bimetallic and Sulfidated Nanoscale Zero-Valent Iron. *Environ. Sci. Technol.* **2018**, *52*, 8627–8637.
- (19) Xu, J.; Wang, Y.; Weng, C.; Bai, W.; Jiao, Y.; Kaegi, R.; Lowry, G. V. Reactivity, Selectivity, and Long-Term Performance of Sulfidized Nanoscale Zerovalent Iron with Different Properties. *Environ. Sci. Technol.* **2019**, *53*, 5936–5945.
- (20) Fan, D.; O'Brien Johnson, G.; Tratnyek, P. G.; Johnson, R. L. Sulfidation of Nano Zerovalent Iron (nZVI) for Improved Selectivity During In-Situ Chemical Reduction (ISCR). *Environ. Sci. Technol.* **2016**, *50*, 9558–9565.
- (21) Su, Y.; Jassby, D.; Song, S.; Zhou, X.; Zhao, H.; Filip, J.; Petala, E.; Zhang, Y. Enhanced Oxidative and Adsorptive Removal of Diclofenac in Heterogeneous Fenton-Like Reaction with Sulfide Modified Nanoscale Zerovalent Iron. *Environ. Sci. Technol.* **2018**, *52*, 6466–6475.
- (22) Cao, Z.; Li, H.; Xu, X.; Xu, J. Correlating Surface Chemistry and Hydrophobicity of Sulfidized Nanoscale Zerovalent Iron with its Reactivity and Selectivity for Denitration and Dechlorination. *Chem. Eng. J.* **2020**, *394*, No. 124876.
- (23) Qin, H.; Guan, X.; Bandstra, J. Z.; Johnson, R. L.; Tratnyek, P. G. Modeling the Kinetics of Hydrogen Formation by Zerovalent Iron: Effects of Sulfidation on Micro- and Nano-Scale Particles. *Environ. Sci. Technol.* **2018**, *52*, 13887–13896.
- (24) Li, J.; Zhang, X.; Sun, Y.; Liang, L.; Pan, B.; Zhang, W.; Guan, X. Advances in Sulfidation of Zerovalent Iron for Water Decontamination. *Environ. Sci. Technol.* **2017**, *51*, 13533–13544.
- (25) Wei, X.; Yin, H.; Peng, H.; Chen, R.; Lu, G.; Dang, Z. Reductive Debromination of Decabromodiphenyl Ether by Iron Sulfide-Coated Nanoscale Zerovalent Iron: Mechanistic Insights From Fe(II) Dissolution and Solvent Kinetic Isotope Effects. *Environ. Pollut.* **2019**, *253*, 161–170.
- (26) He, F.; Gong, L.; Fan, D.; Tratnyek, P. G.; Lowry, G. V. Quantifying the Efficiency and Selectivity of Organohalide Dechlorination by Zerovalent Iron. *Environ. Sci.: Processes Impacts* **2020**, *22*, 528–542.

- (27) Xu, J.; Cao, Z.; Zhou, H.; Lou, Z.; Wang, Y.; Xu, X.; Lowry, G. V. Sulfur Dose and Sulfidation Time Affect Reactivity and Selectivity of Post-Sulfidized Nanoscale Zerovalent Iron. *Environ. Sci. Technol.* **2019**, *53*, 13344–13352.
- (28) Xu, J.; Avellan, A.; Li, H.; Liu, X.; Noël, V.; Lou, Z.; Wang, Y.; Kaegi, R.; Henkelman, G.; Lowry, G. V. Sulfur Loading and Speciation Control the Hydrophobicity, Electron Transfer, Reactivity, and Selectivity of Sulfidized Nanoscale Zerovalent Iron. *Adv. Mater.* **2020**, *32*, No. 1906910.
- (29) Xu, W.; Li, Z.; Shi, S.; Qi, J.; Cai, S.; Yu, Y.; O. Carroll, D. M.; He, F. Carboxymethyl Cellulose Stabilized and Sulfidated Nanoscale Zero-Valent Iron: Characterization and Trichloroethene Dechlorination. *Appl. Catal., B* **2020**, *262*, No. 118303.
- (30) Lv, D.; Zhou, J.; Cao, Z.; Xu, J.; Liu, Y.; Li, Y.; Yang, K.; Lou, Z.; Lou, L.; Xu, X. Mechanism and Influence Factors of Chromium-(VI) Removal by Sulfide-Modified Nanoscale Zerovalent Iron. *Chemosphere* **2019**, *224*, 306–315.
- (31) Dong, H.; Zhang, C.; Deng, J.; Jiang, Z.; Zhang, L.; Cheng, Y.; Hou, K.; Tang, L.; Zeng, G. Factors Influencing Degradation of Trichloroethylene by Sulfide-Modified Nanoscale Zero-Valent Iron in Aqueous Solution. *Water Res.* **2018**, *135*, 1–10.
- (32) Wang, B.; Dong, H.; Li, L.; Wang, Y.; Ning, Q.; Tang, L.; Zeng, G. Influence of Different Co-Contaminants on Trichloroethylene Removal by Sulfide-Modified Nanoscale Zero-Valent Iron. *Chem. Eng. J.* **2020**, *381*, No. 122773.
- (33) Rayaroth, M. P.; Prasanthkumar, K. P.; Kang, Y.; Lee, C.; Chang, Y. Degradation of Carbamazepine by Singlet Oxygen from Sulfidized Nanoscale Zero-Valent Iron – Citric Acid System. *Chem. Eng. J.* **2020**, *382*, No. 122828.
- (34) Xu, W.; Hu, X.; Lou, Y.; Jiang, X.; Shi, K.; Tong, Y.; Xu, X.; Shen, C.; Hu, B.; Lou, L. Effects of Environmental Factors on the Removal of Heavy Metals by Sulfide-Modified Nanoscale Zerovalent Iron. *Environ. Res.* **2020**, *187*, No. 109662.
- (35) Han, Y.; Ghoshal, S.; Lowry, G. V.; Chen, J. A Comparison of the Effects of Natural Organic Matter on Sulfidated and Non-sulfidated Nanoscale Zerovalent Iron Colloidal Stability, Toxicity, and Reactivity to Trichloroethylene. *Sci. Total Environ.* **2019**, *671*, 254–261.
- (36) Fan, D.; Anitori, R. P.; Tebo, B. M.; Tratnyek, P. G.; Lezama Pacheco, J. S.; Kukkadapu, R. K.; Engelhard, M. H.; Bowden, M. E.; Kovarik, L.; Arey, B. W. Reductive Sequestration of Per technetate ( $99\text{TcO}_4^-$ ) by Nano Zerovalent Iron (nZVI) Transformed by Abiotic Sulfide. *Environ. Sci. Technol.* **2013**, *47*, 5302–5310.
- (37) Wu, J.; Zhao, J.; Hou, J.; Zeng, R. J.; Xing, B. Degradation of Tetrabromobisphenol a by Sulfidated Nanoscale Zerovalent Iron in a Dynamic Two-Step Anoxic/Oxic Process. *Environ. Sci. Technol.* **2019**, *53*, 8105–8114.
- (38) Duan, J.; Ji, H.; Liu, W.; Zhao, X.; Han, B.; Tian, S.; Zhao, D. Enhanced Immobilization of U(VI) Using a New Type of FeS-modified  $\text{Fe}^0$  Core-Shell Particles. *Chem. Eng. J.* **2019**, *359*, 1617–1628.
- (39) Wan, H.; Islam, M. S.; Qian, D.; Ormsbee, L.; Bhattacharyya, D. Reductive Degradation of  $\text{CCl}_4$  by Sulfidized Fe and Pd-Fe Nanoparticles: Kinetics, Longevity, and Morphology Aspects. *Chem. Eng. J.* **2020**, *394*, No. 125013.
- (40) Mangayayam, M. C.; Alonso-de-Linaje, V.; Dideriksen, K.; Tobler, D. J. Effects of Common Groundwater Ions on the Transformation and Reactivity of Sulfidized Nanoscale Zerovalent Iron. *Chemosphere* **2020**, *249*, No. 126137.
- (41) Bhattacharjee, S.; Ghoshal, S. Optimal Design of Sulfidated Nanoscale Zerovalent Iron for Enhanced Trichloroethene Degradation. *Environ. Sci. Technol.* **2018**, *52*, 11078–11086.
- (42) Han, Y.; Yan, W. Reductive Dechlorination of Trichloroethene by Zero-Valent Iron Nanoparticles: Reactivity Enhancement through Sulfidation Treatment. *Environ. Sci. Technol.* **2016**, *50*, 12992–13001.
- (43) Zhang, W.; Gao, J.; Duan, W.; Zhang, D.; Jia, J.; Wang, Y. Sulfidated Nanoscale Zero-Valent Iron is an Efficient Material for the Removal and Regrowth Inhibition of Antibiotic Resistance Genes. *Environ. Pollut.* **2020**, *263*, No. 114508.
- (44) Cao, Z.; Xu, J.; Li, H.; Ma, T.; Lou, L.; Henkelman, G.; Xu, X. Dechlorination and Defluorination Capability of Sulfidized Nanoscale Zerovalent Iron with Suppressed Water Reactivity. *Chem. Eng. J.* **2020**, *400*, No. 125900.
- (45) Schoonen, M. A. A.; Xu, Y. The Absolute Energy Positions of Conduction and Valence Bands of Selected Semiconducting Minerals. *Am. Mineral.* **2000**, *85*, 543–556.
- (46) Mangayayam, M.; Dideriksen, K.; Ceccato, M.; Tobler, D. J. The Structure of Sulfidized Zero-Valent Iron by One-Pot Synthesis: Impact on Contaminant Selectivity and Long-Term Performance. *Environ. Sci. Technol.* **2019**, *53*, 4389–4396.
- (47) Song, S.; Su, Y.; Adeleye, A. S.; Zhang, Y.; Zhou, X. Optimal Design and Characterization of Sulfide-Modified Nanoscale Zerovalent Iron for Diclofenac Removal. *Appl. Catal., B* **2017**, *201*, 211–220.
- (48) Xu, J.; Cao, Z.; Liu, X.; Zhao, H.; Xiao, X.; Wu, J.; Xu, X.; Zhou, J. L. Preparation of Functionalized Pd/Fe- $\text{Fe}_3\text{O}_4$ @MWCNTs Nanomaterials for Aqueous 2,4-Dichlorophenol Removal: Interactions, Influence Factors, and Kinetics. *J. Hazard. Mater.* **2016**, *317*, 656–666.
- (49) Xu, J.; Liu, X.; Cao, Z.; Bai, W.; Shi, Q.; Yang, Y. Fast Degradation, Large Capacity, and High Electron Efficiency of Chloramphenicol Removal by Different Carbon-Supported Nanoscale Zerovalent Iron. *J. Hazard. Mater.* **2020**, *384*, No. 121253.
- (50) Liu, Y.; Majetich, S. A.; Tilton, R. D.; Sholl, D. S.; Lowry, G. V. TCE Dechlorination Rates, Pathways, and Efficiency of Nanoscale Iron Particles with Different Properties. *Environ. Sci. Technol.* **2005**, *39*, 1338–1345.
- (51) Mos, Y. M.; Vermeulen, A. C.; Buisman, C. J. N.; Weijma, J. X-Ray Diffraction of Iron Containing Samples: The Importance of a Suitable Configuration. *Geomicrobiol. J.* **2018**, *35*, 511–517.
- (52) Prietzel, J.; Botzaki, A.; Tyufekchieva, N.; Brettholle, M.; Thieme, J.; Klysubun, W. Sulfur Speciation in Soil by S K-Edge XANES Spectroscopy: Comparison of Spectral Deconvolution and Linear Combination Fitting. *Environ. Sci. Technol.* **2011**, *45*, 2878–2886.
- (53) Su, Y.; Adeleye, A. S.; Huang, Y.; Zhou, X.; Keller, A. A.; Zhang, Y. Direct Synthesis of Novel and Reactive Sulfide-Modified Nano Iron through Nanoparticle Seeding for Improved Cadmium-Contaminated Water Treatment. *Sci. Rep.* **2016**, *6*, No. 24358.
- (54) Helm, L.; Merbach, A. E. Inorganic and Bioinorganic Solvent Exchange Mechanisms. *Chem. Rev.* **2005**, *105*, 1923–1960.
- (55) Noël, V.; Boye, K.; Kukkadapu, R. K.; Bone, S.; Lezama Pacheco, J. S.; Cardarelli, E.; Janot, N.; Fendorf, S.; Williams, K. H.; Bargar, J. R. Understanding Controls on Redox Processes in Floodplain Sediments of the Upper Colorado River Basin. *Sci. Total Environ.* **2017**, *603–604*, 663–675.
- (56) Ikogou, M.; Ona-Nguema, G.; Juillot, F.; Le Pape, P.; Menguy, N.; Richeux, N.; Guigner, J.; Noël, V.; Brest, J.; Baptiste, B.; Morin, G. Long-Term Sequestration of Nickel in Mackinawite Formed by *Desulfovibrio Capillatus* upon Fe(III)-citrate Reduction in the Presence of Thiosulfate. *Appl. Geochem.* **2017**, *80*, 143–154.
- (57) Gu, Y.; Gong, L.; Qi, J.; Cai, S.; Tu, W.; He, F. Sulfidation Mitigates the Passivation of Zero Valent Iron at Alkaline pHs: Experimental Evidences and Mechanism. *Water Res.* **2019**, *159*, 233–241.
- (58) Holder, C. F.; Schaak, R. E. Tutorial on Powder X-ray Diffraction for Characterizing Nanoscale Materials. *ACS Nano* **2019**, *13*, 7359–7365.
- (59) Hu, J.; Zhang, Y.; Law, M.; Wu, R. Increasing the Band Gap of Iron Pyrite by Alloying with Oxygen. *J. Am. Chem. Soc.* **2012**, *134*, 13216–13219.
- (60) Van Zeghbroeck, B. *Principles of Semiconductor Devices*; The Oxford Series in Electrical and Computer Engineerings; University of Colorado, 2011.
- (61) Dalven, R. *Empirical Relation between Energy gap and Lattice Constant in Cubic Semiconductors*; Lawrence Berkeley National Laboratory. LBNL Report #: LBL-2218. Retrieved from <https://escholarship.org/uc/item/94w2h9sr>, 1973.